

Mark Konijnenberg

## 2.1 Set-Up Chapter

$^{99m}\text{Tc}$  radiation physics, imaging principles, and standard protocol  
Traditional dosimetry  $^{99m}\text{Tc}$  MIBI, effective dose + dose to gall bladder, etc.  
Additional dose by CT in SPECT/CT  
Comparison to other myocardial imaging procedures  
Consequences of dose and justification of high dose versus benefit  
Physical developments, scatter correction, attenuation correction, resolution improvement, smallest lesions, faster acquisition before liver uptake

### 2.1.1 Radiation Physics $^{99m}\text{Tc}$ -Decay and Imaging Principles

Technetium is an element with only unstable isotopes, although the ground state  $^{99}\text{Tc}$  with a decay half-life of 211,100 years can almost be considered to be stable. With the decay of Molybdenum-99 in a  $^{99}\text{Mo}$ - $^{99m}\text{Tc}$  generator the meta-stable  $^{99m}\text{Tc}$  is formed, which is an isomeric state of  $^{99}\text{Tc}$  (see the decay chart in Fig. 2.1). This isomeric state decays to its ground state  $^{99}\text{Tc}$  with a half-life of 6.015 h. In 89% of all decays, a gamma-ray is released with an energy of 140.5 keV. This gamma-photon is used for imaging of the distribution of the  $^{99m}\text{Tc}$  labeled MIBI inside the patient with a gamma camera. In the decay, not only gamma-rays are emitted but also X-rays, low-energy Auger and internal conversion electrons and  $^{99}\text{Tc}$  itself decays with the emission of beta-rays. The abundance and energy of each decay

---

M. Konijnenberg  
Erasmus MC, Nuclear Medicine Department,  
Rotterdam, The Netherlands  
e-mail: m.konijnenberg@erasmusmc.nl

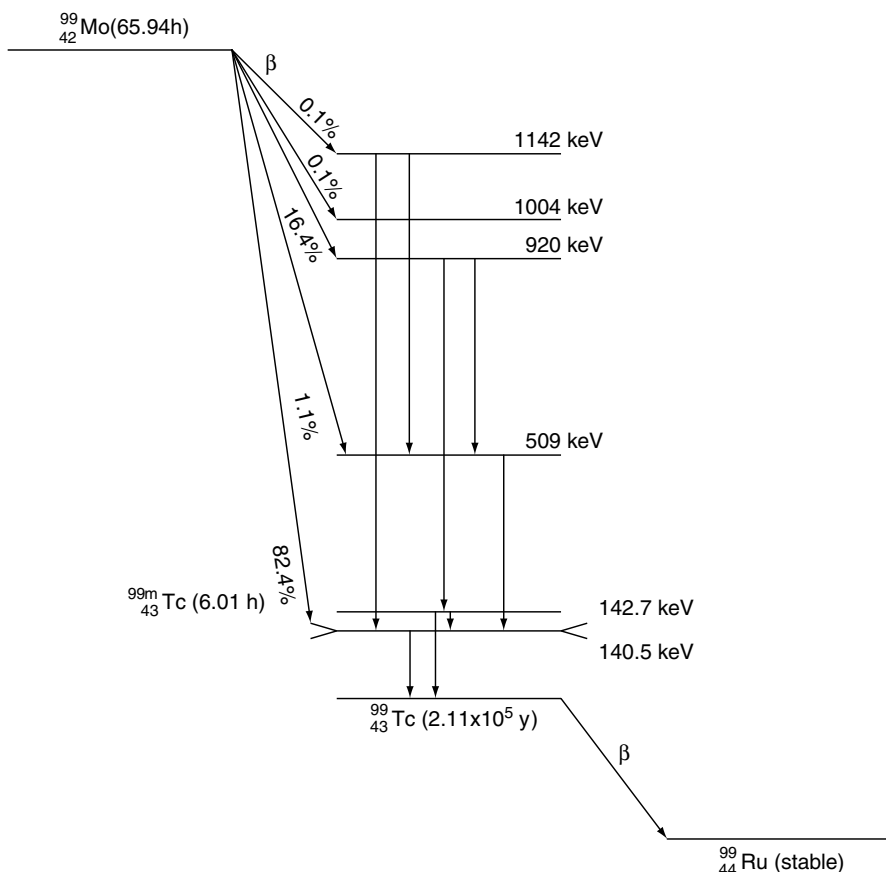


**Fig. 2.1** Decay scheme of  $^{99}\text{Mo}$ , 82.4% decays to the 142.7 keV level of the metastable  $^{99\text{m}}\text{Tc}$  which decays to the 140.5 keV level through internal conversion with a half-life of 6.01 h and this level almost immediately decays to the ground state of  $^{99}\text{Tc}$  under the emission of 140 keV gamma-rays. By contributions from other levels 89.1% is accumulated in the 142.7 keV  $^{99\text{m}}\text{Tc}$  level and emits the 140.5 keV gamma-ray

emission is indicated in Table 2.1. The electrons and beta-rays do not interfere with the image quality of the  $^{99\text{m}}\text{Tc}$ -scan, but do have an influence on the radiation dosimetry of  $^{99\text{m}}\text{Tc}$ -labeled radiopharmaceuticals.

Imaging of radioactivity uptake patterns in patients after injection of  $^{99\text{m}}\text{Tc}$  MIBI is performed with the Anger scintillation camera or simply gamma camera, its schematic principle is shown in Fig. 2.2. When the gamma camera is orbited around the patient, 3-dimensional (3-D) tomographic images can be made of the gamma-rays emitted and hence it is called single photon emission gamma camera tomography, or SPECT for short. Several features in radiation transport physics influence the quality and possibilities of the SPECT imaging which are briefly listed here:

**Table 2.1** Radiation characteristics of  $^{99m}\text{Tc}$  with a half-life of 6.015 h

Radiation	Energy (keV)	Intensity (%/decay)
Conversion electron M	1.6286	74.595
Auger electron L	2.17	10.32
Auger electron K	15.5	2.05
Conversion electron K	119.5	8.84
Conversion electron K	121.6	0.55
Conversion electron L	137.5	1.07
Conversion electron L	139.6	0.172
Conversion electron M	140.0	0.194
Conversion electron NP	140.4	0.0374
Conversion electron M	142.1	0.034
Conversion electron NP	142.6	0.0066
X-ray L	2.42	0.447
X-ray $K\alpha_2$	18.25	2.14
X-ray $K\alpha_1$	18.37	4.07
X-ray $K\beta_3$	20.60	0.330
X-ray $K\beta_1$	20.62	0.639
X-ray $K\beta_2$	21.01	0.145
$\gamma$ -ray	140.511	89.06
$\gamma$ -ray	142.63	0.0187

### 2.1.2 Attenuation

Attenuation of the 140 keV gamma-rays in the body distorts the image. Source regions with more or denser tissue in the path to the detector show more attenuation of the gamma-rays than shallower lying source regions. Several methods have been developed for correction of attenuation in the patient's body. The most simple method is by estimating the thickness of tissue  $d$  through which the photons travel and correcting the raw image data  $I(d)$  with the exponential equation  $I(d) = I_0 e^{-\mu d}$ . The linear attenuation coefficient  $\mu$  for 140 keV gamma-rays in water is: 0.15/cm. The attenuation can be simulated by using a phantom with comparable dimensions of the region of interest and various layers of tissue-like material for attenuation. This method applies well for a source within a homogeneous medium.

In reality, however, patient bodies hardly resemble phantoms and especially the heart region with normal density myocardium surrounded by regions with high density as spine, low density lung, and intermediate density breasts, is hardly like the homogeneous phantom. The attenuation correction cannot be expressed by a constant  $\mu$  factor. Transmission sources can be used to measure the transmission and thus attenuation map along the field of view in the SPECT system. Transmission scans (TCT) and X-ray CT imaging are capable of producing 3-D maps of the attenuation ( $\mu$ -map) in each voxel of the SPECT image and thus provide patient-specific attenuation correction. SPECT/CT systems are therefore increasingly used. When a low current setting is used for the CT imaging it is possible to obtain a good  $\mu$ -map at reasonably low patient dose [1].

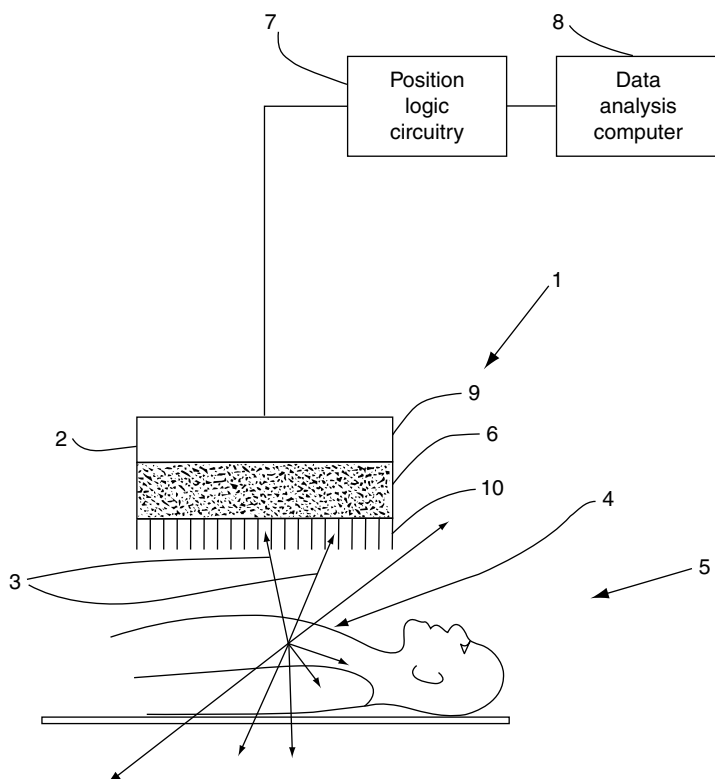


**Fig. 2.2** Schematic view of gamma-camera imaging of the gamma-ray emissions (3) coming from the myocardial regions. The gamma-rays that pass through the collimator (10), generate light pulses in the scintillation crystal (6, usually NaI), which is amplified and transformed into an electronic signal by the photomultiplier tube (9), which signal is then used to determine the source position. When the detector is used at different angles around the patient a 3-D image of the emission distribution can be made

### 2.1.3 Scatter

Scattering of the gamma-rays in the patient not only creates widening of the measured 140 keV energy spectrum, but also scattering from sources neighboring the myocardium, like from the liver, can cause counts within the myocardium region of interest. Apart from scattering in the body, scatter can also occur in the collimator and detector system. Both types of scatter cause deterioration of image resolution. Scatter correction can be solved by using either multiple energy windows on the measured  $^{99m}\text{Tc}$  spectrum to determine the scatter component in the signal empirically [2–4]. The other possibility is to use the  $\mu$ -map and the geometry of the scanner system together with the uncorrected SPECT activity distribution in a Monte Carlo model [5]. This Monte Carlo model can calculate from scatter theory the scatter and photo peak signal contributions in each ROI, as

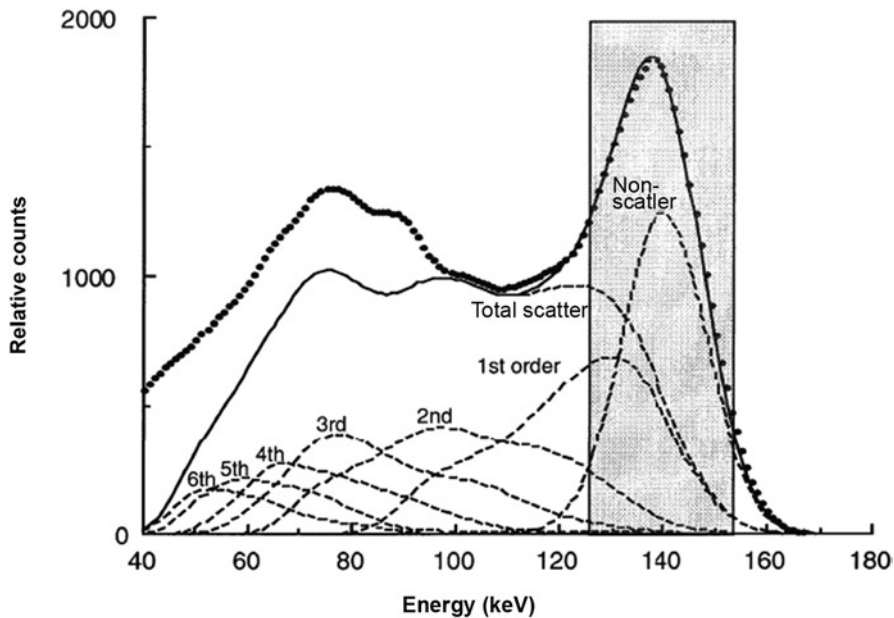


**Fig. 2.3** Energy spectrum for the 140 keV  $^{99m}\text{Tc}$  line source on the axis of a water-filled cylinder simulated using the Monte Carlo method. The spectrum due to primary and scattered photons (solid line) is separated into different contributions (total scattering or different orders of photon scattering). The experimentally measured spectrum is also shown (dots)

shown in Fig. 2.3 [6]. It was found that the field of view of the CT scanner should be larger than that of the SPECT camera, as regions outside may cause scatter effects inside its field of view.

#### 2.1.4 Resolution and Partial Volume Effect

The limited spatial resolution of SPECT imaging cameras (for  $^{99m}\text{Tc}$  in the order of 4 mm) causes serious blurring of the images. For large organs, in comparison to the spatial resolution, this is not really a problem as the signal measured is formed by equilibrium between gamma-rays scattering in and those scattering out of the central region. At the edges of these large regions and in finite regions, however, this equilibrium will not exist and distortions of the image, as shown in Fig. 2.4, will be the result. Filtering of the signal to control the noise tends to even enhance this partial volume effect. The lower uptake values in the inferior LV wall can be attributed to this liver-heart artifact [7]. Correction of this partial volume effect involves the use of CT anatomical information in a Monte Carlo code to determine the spill in and out, but it is prone to induce false-negative results when a real perfusion defect occurs in the inferior wall [8]. Corrections for attenuation, scatter, and partial volume effects are invaluable when myocardial imaging is not only used for qualitative

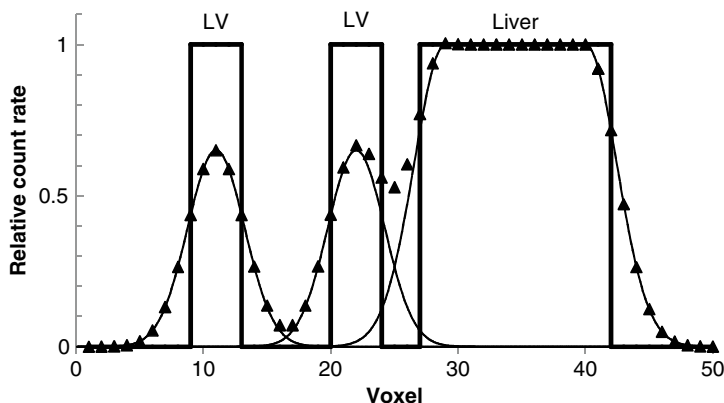


**Fig. 2.4** Partial volume effect by small (just three voxels wide) left ventricle (LV) region next to liver. The *rectangular blocks* show the theoretical activity distribution over liver and LV myocardium. The *dashed curves* show the spill out from each source region due to scatter and limited resolution. In the four voxel thick LV region, partial coverage of these voxels lowers the detector response

diagnosis of possible perfusion defects, but also to measure the magnitude of myocardial perfusion quantitatively.

### 2.1.5 Radiation Dosimetry of $^{99m}\text{Tc}$ MIBI

Myocardial perfusion imaging is the medical imaging procedure with the largest radiation dose to the patient, both on individual basis and on patient-population averaged effective dose per person [9]. The reason it is positioned so high on this list is that the majority of the myocardial imaging procedures in the patient group considered was performed with  $^{201}\text{Tl}$ , which is known to have a high effective dose of 0.14 mSv/MBq in the adult [21], which leads to a mean dose of 16 mSv at the maximum injected activity of 111 MBq. When all myocardial perfusion imaging would have been performed with  $^{99m}\text{Tc}$  MIBI still this procedure would remain in the top contributor segment for annual effective dose together with CT imaging. Theoretically, this high effective dose could cause excess cancer deaths by the radiation, although the individual risk for fatal cancer may be low (approximately 0.02% for a 15 mSv dose given to a 40-year or older patient), when considered over a large patient population the numbers of induced cancers can be substantial [10].

The risk for induction of cancer is assumed to follow a linear relation with the dose given, although it has never been proven below a dose of 100 mSv. This linear no-threshold model for induction of fatal cancer predicts an excess risk of fatal cancer of 0.005% per person per mSv. Still the benefit of the perfusion imaging outweighs the increased risk of cancer induction, as was analyzed by Zanzonico and Stabin for  $^{201}\text{Tl}$  [11]. They stated that 24 mSv by  $^{201}\text{Tl}$  myocardial perfusion imaging would induce fatal cancer in 11 patients over the US heart patient

population, but the procedure would save 109 lives per year by considerably reducing the chance of myocardial infarction during vascular surgery. The net benefit of myocardial perfusion imaging with  $^{201}\text{Tl}$  is 98 lives saved per year. When a  $^{99\text{m}}\text{Tc}$  heart agent would have been used with an effective dose of 15 mSv, the net benefit would rise to 102 lives saved. This clearly makes the high effective dose by myocardial perfusion imaging justifiable, although the ALARA (as low as reasonably achievable) principle in health physics would favor the use of  $^{99\text{m}}\text{Tc}$  heart perfusion agents instead of  $^{201}\text{Tl}$ .

---

## 2.2 Biokinetic of $^{99\text{m}}\text{Tc}$ MIBI

The biokinetic model is summarized in ICRP 80 and based on papers published by Wackers et al. [12], Leide et al. [13] and Boström et al. [14].

MIBI is accumulated in viable myocardial tissue in proportion to regional blood flow, in a manner similar to thallous chloride. After intravenous injection, the substance is rapidly cleared from the blood and taken up predominantly in muscular tissues (including heart). It is accumulated and excreted by liver and kidneys, with a smaller amount; also, an uptake in the salivary glands and thyroid occurs. Other organs and tissues show a low uptake with a uniform distribution. The principal metabolic pathway for excretion is via the hepatobiliary system to the gastrointestinal tract, with some additional excretion via the kidneys. The major part of injected substance is excreted within 48 h [19].

During the first 60 min after an injection in a resting patient, marked accumulation of Sestamibi is present in the liver and spleen; nevertheless, the heart is as well visualized. In conjunction with a stress test, less uptake in the liver and spleen can be observed with a considerable increase of uptake in heart and skeletal muscles. No redistribution takes place, and there is no evidence of any metabolism of the substance [12, 19]. Substantial excretion in the gallbladder was noted both after exercise and at rest, reaching a maximum at circa 1 h after injection.

---

## 2.3 Blood Clearance

Pre- and post-exercise blood decay using clearance curves were measured by Wackers et al. [12].

During rest, at 30 s after injection, blood activity is  $22 \pm 18\%$  of injected activity (IA). Maximal activity of  $36 \pm 18\%$  of IA was noted at 1 min after injection. Blood activity subsequently decreased to  $23 \pm 0.9\%$  of IA at 3 min,  $9 \pm 0.6\%$  at 5 min, and  $2.5 \pm 0.3\%$  of IA at 10 min after injection. After this time, MIBI blood clearance continues to decrease slowly. At 60 min,  $0.8 \pm 0.02\%$  of IA are reached, at 2 h  $0.5 \pm 0.03\%$  of IA, at 4 h p.i. At 24 h, blood activity was  $0.3 \pm 0.004\%$  of IA. Curve fitting through the data shows that in rest mibi clears bi-exponentially from the blood:  $41.9 \pm 0.1\%$  with a clearance half-life of  $1.37 \pm 0.03$  min and  $1.28 \pm 0.05\%$

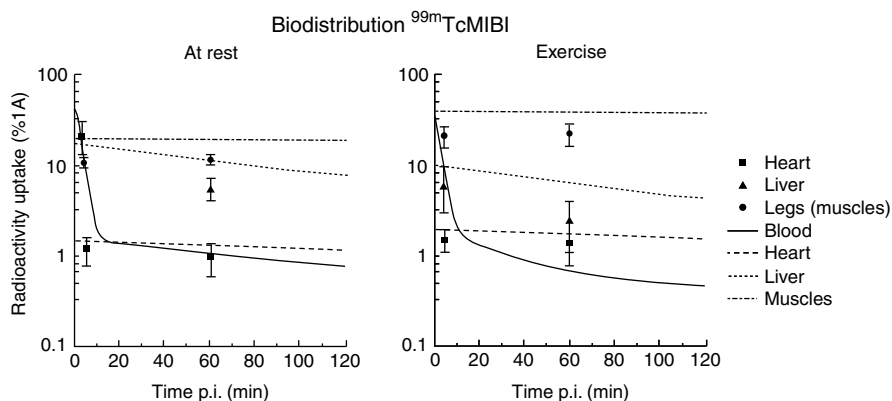


**Fig. 2.5** Biodistribution patterns for  $^{99m}\text{Tc}$  MIBI injected at rest and injected under peak stress exercise. The data points for heart, liver, and legs were taken from Wackers et al [12]. The blood curves were fitted through the blood data from Wackers. The curves for heart, liver, and muscle were taken from ICRP80 [19] and are substantially higher than the data

with a half-life of  $88 \pm 9$  min. These values are different from the curves presented by Wackers. There it was claimed that the fast clearance component proceeds with 2.18 min effective half-life, whereas the curve presented indicated a 19 s half-life (Fig. 2.5).

During exercise, maximal MIBI blood activity ( $51 \pm 28\%$  of IA) was measured at 0.5 min. Blood activity decreased over the following minutes, reaching a level of  $11 \pm 4\%$  of IA at 4 min,  $6.5 \pm 2.9\%$  of IA at 5 min, and  $2.6 \pm 1\%$  of IA at 10 min after injection. Thereafter, blood pool activity continued to decrease slowly:  $1.1 \pm 0.1\%$  of IA at 30 min,  $0.7 \pm 0.1\%$  of IA at 1 h,  $0.4 \pm 0.2\%$  of IA at 4 h, and  $0.3 \pm 0.3\%$  of IA at 24 h after injection. The blood clearance with exercise proceeds with 3 compartments:  $58 \pm 36\%$  with a clearance half-life of  $1.5 \pm 0.5$  min,  $1.8 \pm 0.9\%$  with  $T_{1/2} = 22 \pm 16$  min, and  $0.44 \pm 0.10\%$  with  $T_{1/2} = 41$  h. Again, this blood curve differs from the curve originally presented.

## 2.4 Upper-Body Organ Distribution

Under resting conditions, initially, the highest MIBI concentration was in gallbladder and liver, followed in decreasing order of activity per pixel, by heart, spleen, and lungs. Decay corrected MIBI activity in spleen and lung decreased gradually over time, whereas MIBI activity in the heart remained relatively stable. At 3 h after injection  $27 \pm 4\%$  of initial activity had cleared from the heart, whereas  $67 \pm 12\%$ ,  $76 \pm 4\%$ , and  $49 \pm 4\%$  had, respectively, cleared from spleen, liver, and lungs. Within the first 30–60 min, liver activity decreased with excretion into the biliary system, maximal accumulation in the gallbladder occurred at approximately 60 min p.i. Consequently, since no significant redistribution of MIBI occurs, with regard to laboratory logistics and patient flow, a convenient and practical time for imaging is



approximately 1 h after injection. However, with increasing time interval between injection and scan, the relative visualization of the heart will continue to improve.

During exercise, immediately after injection, the highest concentration of MIBI was in the gallbladder, followed by heart, liver, spleen, and lungs. Again, the cardiac, pulmonary, and spleen activity gradually decreased over time. Hepatic activity decreased more rapidly due to excretion in the biliary system. By 3 h after injection,  $26 \pm 12\%$  of initial cardiac activity had cleared; at this time,  $65 \pm 7\%$  had cleared from the liver,  $43 \pm 21\%$  from the spleen, and  $39 \pm 10\%$  from the lungs. The count density within the heart was higher than in the immediately adjacent organs. Only the gallbladder had higher count density.

A pharmacokinetic compartment model for  $^{99m}\text{Tc}$  MIBI is unfortunately missing. This would support more clearly the additional compartment found in the blood clearance with exercise. Also, the liver uptake kinetics would be better described, thus giving better arguments for doing early myocardial uptake scanning with high speed *czt* detectors [15]. These experiments indicate that the uptake in the liver proceeds much slower than the myocardial uptake, thus creating an early opportunity for imaging, contrary to the traditional scanning time a half to 1 h after injection.

---

## 2.5 Heart-to-Organ Ratios

Wackers et al. (1989) have summarized the heart/liver, heart/lung, and heart/spleen ratios in humans after 5 up to 180 min post injection. For example, the 60 min ratios increased from  $0.6 \pm 0.1$  (rest) to  $1.8 \pm 0.3$  (exercise) for heart and liver, these figures were  $2.4 \pm 0.1$  (rest and exercise) for heart/lung, and  $1.3 \pm 0.3$  (rest) and  $2.5 \pm 0.3$  (exercise) for the heart/spleen ratio.

The data for organ dosimetry were summarized in ICRP 80 and in the paper published by Wackers et al. (1989): in general, organ dosimetry was determined from whole body images by expressing specific organ uptake as percent of injected dose. The 24-h urinary excretion was 29.5% of IA at rest and 24.1% of IA after exercise. The 48-h fecal excretion was 36.9% of IA at rest and 29.1% of ID after exercise.

According to Leide et al. (1992), there is a significant difference in the biodistribution of MIBI between stress and rest for the following tissues: muscle tissue, thyroid, gall bladder, and remaining tissues. The activity content in the small intestine, upper large intestine, and lower large intestine also differs between stress and rest. Since the uptake in the muscle tissue is lower at rest compared to stress, the substance reaches the GI-tract earlier at rest than stress. That is why the content in ULI (upper large intestine) is higher 6 h after injection at rest than stress. It is the same reason why the content in ULI at 24 h is lower at rest. By then the substance has already reached the LLI (lower large intestine).

In conclusion, it can be summarized, that the major metabolic pathway for clearance of Sestamibi is the hepatobiliary system. Activity from the gallbladder appears in the intestine within 1 h of injection (after exercise and at rest). About 27% of the ID is cleared through renal elimination after 24 h and approximately 33% of the ID is cleared through the feces in 48 h.

## 2.6 Radiation Dosimetry

The effect of radiation exposure in tissue can be expressed by the absorbed dose. Absorbed dose  $D$  is defined as the mean absorbed energy  $\bar{E}$  in a target region or organ coming from a source region, divided by the mass  $m$  of the target organ:

$$D = \frac{dE(\text{target} \leftarrow \text{source})}{dm_{\text{target}}}$$

The unit of the dose is J/kg or Gray [Gy], in older literature the unit rad is used for dose with the conversion 1 rad = 0.01 Gy. In radionuclide dosimetry the convention to calculate the absorbed dose is by the MIRD-formalism. It makes a division between the kinetics of the radiopharmaceutical distribution and the static part of absorption of the radionuclide's specific energy from source to target combination. The dose rate  $\dot{D}(t)$  per activity  $A$ , both as function of time  $t$ , for a source-to-target combination can be written as:

$$\frac{\dot{D}(t)}{A(t)} = \frac{k \sum_i y_i E_i \phi_i(\text{target} \leftarrow \text{source})}{m_{\text{target}}} = S(\text{target} \leftarrow \text{source})$$

With  $k$  a conversion factor from MeV/g to Gy

$$(\text{usually } k = 0.16022 \frac{\text{mGy}}{\text{MBq.s}} / \frac{\text{MeV}}{\text{g.decay}} \text{ is used}),$$

$y_i$  is the yield per decay of gamma-rays with energy  $E_i$  (for  $^{99\text{m}}\text{Tc}$  see Table 2.1) and  $\phi_i$  is the absorbed fraction of energy in the target organ for a gamma-ray with energy  $E_i$  coming from the source organ. The kinetic part of the equation is on the left side, and the static physics part, specific for the radionuclide of interest, is on the right side of the equation. For diagnostically used radionuclides, this physics part, often called S-value or absorbed dose factor, is calculated for reference stylized phantom models, like the MIRD phantoms, with Monte Carlo radiation transport codes. Several dosimetry codes exist that provide S-values for all conventionally used radionuclides and all possible source-to-target organ combinations, like Olinda/EXM [16]. Dosimetry for therapeutic use should be based on patient-specific geometry and not on phantom models.

The kinetic part of the dose rate equation is solved by using the biokinetic distribution of the radiopharmaceutical. The total number of decays that yield an absorbed gamma-ray in the target organ is calculated by integration of the time-activity curve multiplied with the S-value:

$$D = \int_0^{\infty} A(t) e^{-\lambda t} dt \times S(\text{target} \leftarrow \text{source}) = \tilde{A}_{\text{target}} \times S(\text{target} \leftarrow \text{source})$$

**Table 2.2** Tissue weighting factors  $w_T$  for calculating the effective dose, according to ICRP publications 60 [18] and 103 [20]

Tissue	Tissue weighting factor, $w_T$		
	ICRP26	ICRP60	ICRP103
Bone surfaces	0.03	0.01	0.01
Bladder		0.05	0.04
Brain			0.01
Breast	0.15	0.05	0.12
Colon		0.12	0.12
Gonads	0.25	0.20	0.08
Liver		0.05	0.04
Lungs	0.12	0.12	0.12
Eesophagus		0.05	0.04
Red bone marrow	0.12	0.12	0.12
Salivary glands			0.01
Skin		0.01	0.01
Stomach		0.12	0.12
Thyroid	0.03	0.05	0.04
Remainder	0.3	0.05	0.12
Total	1.0	1.0	1.0

With  $\lambda$  the decay constant of the radionuclide (for  $^{99m}\text{Tc}$ :  $\lambda = \ln(2)/6.015 = 0.1152/h$ ), when  $A(t)$  is the decay corrected time-activity curve, and  $\tilde{A}$  the cumulated activity in a source organ. Often the cumulated activity per injected activity ( $\tilde{A}/IA$ ) is indicated as organ residence time  $\tau$ . The advantage of this division into kinetic and static part is that the dosimetry can easily be updated with improved calculational models for the static part. The limitations of this model, however, show up when the activity is heterogeneously distributed over the source organ, or when the source and target organ are variable in size, like a rapidly growing tumor.

To enable dose comparisons of different radiation exposures, specifically meant for radiation protection and dose limits for health physics in radiation work situation, the effective dose has been introduced by the ICRP [18]. The effective dose  $E$  is a weighted mean organ dose, with weights  $w_T$  assigned to each organ expressing its radiosensitivity for induction of fatal cancer or genetic damage:

$$E = \sum_T w_T \sum_R w_R D_{T,R}$$

With  $w_T$  the organ or tissue weighting factors, listed in Table 2.2, expressing the relative risk for late radiation effects in these tissues, and  $w_R$  the radiation weighting factor, which is 1 for all low LET radiation like gamma-rays and beta-particles, expressing the relative risk associated with high LET radiation. For  $^{99m}\text{Tc}$ , therefore, only the first summation over the weighted organ doses  $D_T$  is of relevance, as  $w_R = 1$  for all LET radiation. The unit for effective dose is the Sievert, or Sv. In older literature rem is used instead of Sv (with 1 rem = 0.01 Sv). Also the definition of effective dose has changed with increasing knowledge of tissue radiosensitivities. With tissue

weighting factors according to ICRP26 [17], effective dose equivalents were defined. Although the differences for  $^{99m}\text{Tc}$  MIBI are not large, care should be taken in comparing equally defined effective doses.

The radiation dosimetry for  $^{99m}\text{Tc}$  MIBI is based on the evaluation in ICRP publication 80 [19]. The biokinetic model is based on the old work by Wackers and by Leide et al. As already shown in the paragraph on biodistribution of MIBI, these reports could be much improved and the dose values given can therefore be taken as approximate values, mere estimates of the dose magnitude. The dose tables indicate dose estimates for each organ and the effective dose according to ICRP60. The effective dose indicates the weighted average organ dose, with weights indicating the susceptibility of each separate organ to radiation-induced cancer. The effective dose is a tool to enable comparisons between different types of radiation exposure, especially in health physics. The newer organ weights from ICRP publication 103 do not alter the effective dose for  $^{99m}\text{Tc}$  MIBI significantly [22].

The maximum dose is reached in the gallbladder, both for the rest and the exercise studies (Tables 2.3 & 2.4). Also, the kidneys and colon get higher doses than average. In comparison to the effective dose per activity by  $^{201}\text{Tl}$  of 0.14 mSv/MBq, with the highest organ dose in the kidneys (0.48 mGy/MBq),  $^{99m}\text{Tc}$  MIBI has a 15-fold lower dose (ICRP publication 106 2008). For that reason  $^{201}\text{Tl}$  is used at much lower activities than  $^{99m}\text{Tc}$  MIBI: typically 75 MBq for a stress test instead of 1,000 MBq  $^{99m}\text{Tc}$  MIBI used. The effective dose from 75 MBq  $^{201}\text{Tl}$  is 11 mSv, whereas 1,000 MBq  $^{99m}\text{Tc}$  MIBI gives an effective dose of 8 mSv. The doses to each organ for a rest study with 500 MBq  $^{99m}\text{Tc}$  MIBI and an exercise study with 1,000 MBq  $^{99m}\text{Tc}$  MIBI (1-day protocol) are given in Tables 2.5 and 2.6.

Although the dose tables suggest that the pediatric doses are known, it is in reality the result of using unchanged adult biokinetics to children in child-size calculational phantoms. No studies were made to confirm that the biodistribution of  $^{99m}\text{Tc}$  MIBI in children is equal to the adult situation. Qualitatively, however, no differences have been observed between adult and pediatric myocardial uptake. The recommended activities for  $^{99m}\text{Tc}$  MIBI show huge variations in dose reference levels for each country. To make a comparison possible, the maximum activity in clinical practice is taken as example: a 1-day protocol with 500 MBq  $^{99m}\text{Tc}$  MIBI at rest and then 1,000 MBq  $^{99m}\text{Tc}$  MIBI in an exercise test. These activities are for an adult. The EANM pediatrics committee published recommendations for the dosage of radiopharmaceuticals in children [23]. For  $^{99m}\text{Tc}$  MIBI the minimum activity is 80 MBq and the baseline activity for a rest test is 28 MBq and for a stress test it is 84 MBq. These baseline activities must be multiplied with body weight-dependent multiples. The pediatric injected activities in Tables 2.5 and 2.6 were calculated accordingly, using the MIRD phantom body weights of 57, 33, 20, and 10 kg for a 15-, 10-, 5-, and 1-year-old, respectively. The weight of the adult (male) phantom is 74 kg and is conservatively chosen, as the dose is inversely proportional with the weight.

With multimodality imaging, the patients will also receive an additional radiation dose from the other imaging modality, when based on radiation of course. With SPECT/CT imaging low-dose setting of the CT-imaging can be used when the CT image is intended for attenuation correction, then the additional effective dose will be in the order of 0.4–0.9 mSv [1]. When the CT image is to be used for

**Table 2.3** Radiation dosimetry table for  $^{99m}\text{Tc}$  MIBI in a resting subject from ICRP80 [19]

Dose per activity (mGy/MBq)	Adult	15 years	10 years	5 years	1 year
Adrenals	0.0075	0.0099	0.015	0.022	0.038
Bladder	0.011	0.014	0.019	0.023	0.041
Bone surfaces	0.0082	0.01	0.016	0.021	0.038
Brain	0.0052	0.0071	0.011	0.016	0.027
Breast	0.0038	0.0053	0.0071	0.011	0.02
Gall bladder	0.039	0.045	0.058	0.1	0.32
GI tract					
Stomach	0.0065	0.009	0.015	0.021	0.035
SI	0.015	0.018	0.029	0.045	0.08
Colon	0.024	0.031	0.05	0.079	0.15
Heart	0.0063	0.0082	0.012	0.018	0.03
Kidneys	0.036	0.043	0.059	0.085	0.15
Liver	0.011	0.014	0.021	0.03	0.052
Lungs	0.0046	0.0064	0.0097	0.014	0.025
Muscles	0.0029	0.0037	0.0054	0.0076	0.014
Esophagus	0.0041	0.0057	0.0086	0.013	0.023
Ovaries	0.0091	0.012	0.018	0.025	0.045
Pancreas	0.0077	0.01	0.016	0.024	0.039
Red marrow	0.0055	0.0071	0.011	0.03	0.044
Salivary glands	0.014	0.017	0.022	0.015	0.026
Skin	0.0031	0.0041	0.0064	0.0098	0.019
Spleen	0.0065	0.0086	0.014	0.02	0.034
Testes	0.0038	0.005	0.0075	0.011	0.021
Thymus	0.0041	0.0057	0.0086	0.013	0.023
Thyroid	0.0053	0.0079	0.012	0.024	0.045
Uterus	0.0078	0.01	0.015	0.022	0.038
Remaining organs	0.0031	0.0039	0.006	0.0088	0.016
Effective dose (mSv/MBq)	0.0090	0.012	0.018	0.028	0.053

The absorbed dose per unit administered activity is given for different age groups, as well as the effective dose [18]

high-resolution CT imaging of the Coronary Arteries (CTCA) effective doses around 15–20 mSv have been reported with high current 64-slice CTCA (A Einstein 2007). Using ECG-controlled current modulation and by adequately adjusting the tube current to the patient's size, high-resolution CTCA can be performed at doses between 5 and 10 mSv. Especially, the effective dose by CT imaging of young children is of great concern [24], but by using appropriate camera setting it is possible to obtain good quality CT scans in children with minimally a 74% reduction in chest doses to around 5 mGy [25].

Combination of 600 MBq  $^{99m}\text{Tc}$  MIBI stress test with 185 MBq  $^{18}\text{F}$  FDG delivers an effective dose of 8.3 mSv (4.7 mSv from  $^{99m}\text{Tc}$  MIBI and 3.5 mSv from  $^{18}\text{F}$  FDG [21]) to the adult patient. When combined with CT the total effective dose to this patient will be 13 mSv. Doses from other PET and SPECT radionuclide myocardial perfusion agents are compared in Table 2.7.

**Table 2.4** Radiation dosimetry table for  $^{99m}\text{Tc}$  MIBI injected at peak stress from ICRP80 [19]

Dose per activity (mGy/MBq)	Adult	15 years	10 years	5 years	1 year
Adrenals	0.0066	0.0087	0.013	0.019	0.033
Bladder	0.0098	0.013	0.017	0.021	0.038
Bone surfaces	0.0078	0.0097	0.014	0.02	0.036
Brain	0.0044	0.006	0.0093	0.014	0.023
Breast	0.0034	0.0047	0.0062	0.0097	0.018
Gall bladder	0.033	0.038	0.049	0.086	0.26
GI tract					
Stomach	0.0059	0.0081	0.013	0.019	0.032
Small intestine	0.012	0.015	0.024	0.037	0.066
Colon	0.019	0.025	0.041	0.064	0.12
Heart	0.0072	0.0094	0.01	0.021	0.035
Kidneys	0.026	0.032	0.044	0.063	0.11
Liver	0.0092	0.012	0.018	0.025	0.044
Lungs	0.0044	0.006	0.0087	0.013	0.023
Muscles	0.0032	0.0041	0.006	0.009	0.017
Esophagus	0.004	0.0055	0.008	0.012	0.023
Ovaries	0.0081	0.011	0.015	0.023	0.04
Pancreas	0.0069	0.0091	0.014	0.021	0.035
Red marrow	0.005	0.0064	0.0095	0.013	0.023
Salivary glands	0.0092	0.011	0.0015	0.002	0.0029
Skin	0.0029	0.0037	0.0058	0.009	0.017
Spleen	0.0058	0.0076	0.012	0.017	0.03
Testes	0.0037	0.0048	0.0071	0.011	0.02
Thymus	0.004	0.0055	0.008	0.012	0.023
Thyroid	0.0044	0.0064	0.0099	0.019	0.035
Uterus	0.0072	0.0093	0.014	0.02	0.035
Remaining organs	0.0033	0.0043	0.0064	0.0098	0.018
Effective dose (mSv/MBq)	0.0079	0.010	0.016	0.023	0.045

The dose per unit administered activity is given for different age groups, as well as the effective dose [18]

**Table 2.5** Radiation doses for  $^{99m}\text{Tc}$  MIBI procedures in a resting subject

Injected activity (MBq):	500	336	204	136	80
Dose per procedure (mGy):	Adult	15 years	10 years	5 years	1 year
Adrenals	3.8	3.3	3.1	3.0	3.0
Bladder	5.5	4.7	3.9	3.1	3.3
Bone surfaces	4.1	3.4	3.3	2.9	3.0
Brain	2.6	2.4	2.2	2.2	2.2
Breast	1.9	1.8	1.4	1.5	1.6
Gall bladder	20	15	12	14	26
GI tract					
Stomach	3.3	3.0	3.1	2.9	2.8
Small intestine	7.5	6.0	5.9	6.1	6.4
Colon	12	10	10	11	12
Heart	3.2	2.8	2.4	2.4	2.4
Kidneys	18	14	12	12	12
Liver	5.5	4.7	4.3	4.1	4.2
Lungs	2.3	2.2	2.0	1.9	2.0
Muscles	1.5	1.2	1.1	1.0	1.1
Esophagus	2.1	1.9	1.8	1.8	1.8
Ovaries	4.6	4.0	3.7	3.4	3.6
Pancreas	3.9	3.4	3.3	3.3	3.1
Red marrow	2.8	2.4	2.2	4.1	3.5
Salivary glands	7.0	5.7	4.5	2.0	2.1
Skin	1.6	1.4	1.3	1.3	1.5
Spleen	3.3	2.9	2.9	2.7	2.7
Testes	1.9	1.7	1.5	1.5	1.7
Thymus	2.1	1.9	1.8	1.8	1.8
Thyroid	2.7	2.7	2.4	3.3	3.6
Uterus	3.9	3.4	3.1	3.0	3.0
Remaining organs	1.6	1.3	1.2	1.2	1.3
Effective dose (mSv)	4.5	4.0	3.7	3.8	4.2

The absorbed dose and administered activity is given for different age groups, as well as the effective dose [18]

**Table 2.6** Radiation doses for  $^{99m}\text{Tc}$  MIBI procedures in stress tests

Injected activity (MBq):	1,000	1,000	612	408	228
Dose per procedure (mGy):	Adult	15 years	10 years	5 years	1 year
Adrenals	6.6	8.7	8.0	7.8	7.5
Bladder	9.8	13	10	8.6	8.7
Bone Surfaces	7.8	9.7	8.6	8.2	8.2
Brain	4.4	6.0	5.7	5.7	5.2
Breast	3.4	4.7	3.8	4.0	4.1
Gall bladder	33	38	30	35	59
GI tract					
Stomach	5.9	8.1	8.0	7.8	7.3
Small intestine	12	15	15	15	15
Colon	19	25	25	26	27
Heart	7.2	9.4	6.1	8.6	8.0
Kidneys	26	32	27	26	25
Liver	9.2	12	11	10	10
Lungs	4.4	6.0	5.3	5.3	5.2
Muscles	3.2	4.1	3.7	3.7	3.9
Esophagus	4.0	5.5	4.9	4.9	5.2
Ovaries	8.1	11	9.2	9.4	9.1
Pancreas	6.9	9.1	8.6	8.6	8.0
Red marrow	5.0	6.4	5.8	5.3	5.2
Salivary glands	9.2	11	0.9	0.8	0.7
Skin	2.9	3.7	3.6	3.7	3.9
Spleen	5.8	7.6	7.3	6.9	6.8
Testes	3.7	4.8	4.3	4.5	4.6
Thymus	4.0	5.5	4.9	4.9	5.2
Thyroid	4.4	6.4	6.1	7.8	8.0
Uterus	7.2	9.3	8.6	8.2	8.0
Remaining organs	3.3	4.3	3.9	4.0	4.1
Effective dose (mSv)	7.9	10	9.8	9.4	10

The absorbed dose and administered activity is given for different age groups, as well as the effective dose [18]

**Table 2.7** Dose estimates for myocardial perfusion imaging with radiopharmaceuticals

Radiopharmaceutical	IA rest (MBq)	IA stress (MBq)	Effective dose (mSv)
$^{99m}\text{Tc}$ MIBI	500	1,000	12.4
$^{99m}\text{Tc}$ Tetrofosmin	500	1,000	10.4
$^{201}\text{Tl}$		75	10.5
$^{99m}\text{Tc}$ MIBI + $^{201}\text{Tl}$ SDI	500 MBq $^{99m}\text{Tc}$ MIBI	75 MBq $^{201}\text{Tl}$	14.5
$^{82}\text{Rb}$	1,500	1,500	10.2
$^{13}\text{N}$ Ammonia	500	500	2.0
$^{15}\text{O}$ Water	1,100	1,100	2.4
$^{18}\text{F}$ FDG	275		5.2



## 2.7 Radiation Exposure from Myocardial Perfusion Agents

The staff in a nuclear medicine department will be inevitably exposed to the radiation coming from the patients. The exposure rates from patients have been worked out by several authors [26, 27]. Per  $^{99m}\text{Tc}$  MIBI procedure with an injected activity of 740 MBq at mean dose to the nuclear medicine technician of  $1.7 \pm 1.0 \mu\text{Sv}$  was measured. With 500 MBq  $^{18}\text{F}$  FDG, the dose to the technician is higher  $5.9 \pm 1.2 \mu\text{Sv}$ . In a PET center handling  $^{18}\text{F}$  FDG,  $^{13}\text{N}$  Ammonia, and  $^{11}\text{C}$  labeled compounds, the average dose to a technologist, handling 831 MBq activity per day, was measured to be  $14 \mu\text{Sv}$ .

## Reference

1. Preuss R, Weise R, Lindner O, Fricke E, Fricke H, Burchert W (2008) Optimisation of protocol for low dose CT-derived attenuation correction in myocardial perfusion SPECT imaging. *Eur J Nucl Med Mol Imaging* 35:1133–1141. doi:10.1007/s00259-007-0680-2
2. Narayanan MV, Pretorius PH, Dahlberg ST (2003) Evaluation of scatter compensation strategies and their impact on human detection performance Tc-99m myocardial perfusion imaging. *IEEE trans Nucl Sci* 50:1522–1527
3. Gur YS, Farncombe TH, Pretorius PH (2002) Comparison of scatter compensation strategies for myocardial perfusion imaging using Tc-99m labeled Sestamibi. *IEEE Trans Nucl Sci* 49:2309–2314
4. Ogawa K, Harata Y, Ichihara T, Kubo A, Hashimoto S (1991) A practical method for position-dependent Compton-scatter correction in single photon emission CT. *IEEE Trans Med Imaging* 10:408–412. doi:10.1109/42.97591
5. Xiao J, de Wit TC, Staelens SG, Bezekman FJ (2006) Evaluation of 3D Monte Carlo-based scatter correction for 99mTc cardiac perfusion SPECT. *J Nucl Med* 47:1662–1669
6. Zaidi H, Koral KF (2004) Scatter modelling and compensation in emission tomography. *Eur J Nucl Med Mol Imaging* 31:761–782. doi:10.1007/s00259-004-1495-z
7. Nuyts J, Dupont P, Van den Maegdenbergh V, Vleugels S, Suetens P, Mortelmans L (1995) A study of the liver-heart artifact in emission tomography. *J Nucl Med* 36:133–139
8. Pretorius PH, King MA (2009) Diminishing the impact of the partial volume effect in cardiac SPECT perfusion imaging. *Med Phys* 36:105–115
9. Fazal R, Krumholz HM, Wang Y, Ross JS, Chen J, Ting HH, et al (2009) Exposure to low-dose ionizing radiation from medical imaging procedures. *N Engl J Med* 361:849–857. doi:10.1056/NEJMoa0901249
10. Sodickson A, Baeyens PF, Andriole KP, Prevedello LM, Nawfel RD, Hanson R, Khorasani R (2009) Recurrent CT, cumulative radiation exposure, and associated radiation-induced cancer risks from CT of adults. *Radiology* 251:175–184
11. Zanzonico P, Stabin M (2008) Benefits of medical radiation exposures. *Health Phys Soc*. Available at: <http://hps.org/hpspublications/articles/Benefitsofmedradexposures.html>. Accessed on January 1, 2009
12. Wackers FJ, Berman DS, Maddahi J, Watson DD, Beller GA, Strauss HW, et al (1989) Technetium-99m hexakis 2-methoxyisobutyl isonitrile: human biodistribution, dosimetry, safety, and preliminary comparison to thallium-201 for myocardial perfusion imaging. *J Nucl Med* 30:301–311
13. Leide S, Diemer H, Ahlgren L, et al (1992) In vivo distribution and dosimetry of Tc-99m MIBI in man. In: S-Stelson A, Watson EE (eds) Fifth International Radiopharmaceutical Dosimetry Symposium Conf-910529, Oak Ridge Associated Universities, Oak Ridge, TN, pp 483–497

14. Boström P-A, Diemer H, Leide S, Lilja B, Bergqvist D (1993)  $^{99}\text{Tcm}$ -Sestamibi uptake in the leg muscles and in the myocardium in patients with intermittent claudication. *Angiology* 44:971–976
15. Berman DS, Kang X, Tamarappoo B, Wolak A, Hayes SW, Nakazato R, Thomson LE, Kite F, Cohen I, Slomka PJ, Einstein AJ, Friedman JD (2009) Stress thallium-201/rest technetium-99m sequential dual isotope high-speed myocardial perfusion imaging. *JACC Cardiovasc Imaging* 2:273–282
16. Stabin MG, Sparks RB, Crowe E. (2005) OLINDA/EXM: the second-generation personal computer software for internal dose assessment in nuclear medicine. *J Nucl Med* 46: 1023–1027
17. ICRP Publication 26 (1977) Recommendations of the ICRP. *Ann ICRP* 1:3
18. ICRP Publication 60 (1991) The 1990 Recommendations of the International Commission on Radiological Protection. *Ann ICRP* 21, pp 1–3
19. ICRP Publication 80 (1998) Radiation dose to patients from radiopharmaceuticals (Addendum 2 to ICRP Publication 53). *Ann ICRP* 28:107–111
20. ICRP Publication 103 (2007) The 2007 Recommendations of the International Commission on Radiological Protection. *Ann ICRP* 37:2–4
21. ICRP Publication 106 (2008) Radiation dose to patients from radiopharmaceuticals. Addendum 3 to ICRP Publication 53. *Ann ICRP* 38:159–162
22. Einstein AJ, Moser KW, Thompson RC, Cerqueira MD, Henzlova MJ (2007) Radiation dose to patients from cardiac diagnostic imaging. *Circulation* 116:1290–1305. doi:10.1161/CIRCULATIONAHA.107.688101
23. Lassmann M, Biassoni L, Monsieurs M, Franzius C, Jacobs F (2007) The new EANM paediatric dosage card. *Eur J Nucl Med Mol Imaging* 34:796–798. doi:10.1007/s00259-007-0370-0
24. Brenner D, Elliston C, Hall E, Berdon W (2001) Estimated risks of radiation-induced fatal cancer from pediatric CT. *AJR Am J Roentgenol* 176:289–296
25. Singh S, Kalra MK, Moore MA, Shailam R, Liu B, Toth TL, Grant E, Westra SJ (2009) Dose reduction and compliance with pediatric CT protocols adapted to patient size, clinical indication, and number of prior studies. *Radiology* 252:200–208. doi:10.1148/radiol.2521081554
26. Chiesa C, De Sanctis V, Crippa F, Schiavini M, Fraigola CE, Bogni A, Pascali C, Decise D, Marchesini R, Bombardieri E (1997) Radiation dose to technicians per nuclear medicine procedure: comparison between technetium-99m, gallium-67, and iodine-131 radiotracers and fluorine-18 fluorodeoxyglucose. *Eur J Nucl Med* 24:1380–1389
27. Benatar NA, Cronin BF, O'Doherty MJ (2000) Radiation dose rates from patients undergoing PET: implications for technologists and waiting areas. *Eur J Nucl Med* 27:583–589

<sup>99m</sup>Tc-Sestamibi

Clinical Applications

Bucerius, J.; Ahmadzadehfar, H.; Biersack, H.-J. (Eds.)

2012, XI, 194 p., Hardcover

ISBN: 978-3-642-04232-4